Phonon-assisted excitonic absorption in diamond

Kazuki Konishi and Nobuko Naka
Department of Physics, Kyoto University, Kitshirakawa-Oiwake-cho, Sakyo-ku, Kyoto 606-8502, Japan

(Received 22 May 2021; revised 10 September 2021; accepted 20 September 2021; published 30 September 2021)

The phonon-assisted optical transitions of excitons in intrinsic diamond have been investigated theoretically and experimentally. Excellent agreement is indicated between absorption spectra measured and calculated based on the phonon coupling strengths from first-principles calculations using just a single adjustable parameter. Temperature shift and broadening are incorporated via a pseudo-Voigt function analysis developed for the derivative of the experimental absorption spectra. The absorption coefficients of excitons in discrete and continuum states are separated and contributions from different phonon modes are discussed, which enable theoretical derivation of the exceptionally high phonon-assisted radiative rate of excitons in diamond among indirect-gap semiconductors. This study expands the applicability of the second-order perturbation theory involving electron-phonon interactions in materials important for future photonics and power electronics.

DOI: 10.1103/PhysRevB.104.125204

I. INTRODUCTION

Optical transitions in indirect band-gap materials are typically considered insignificant because the effect is weak due to second-order processes involving the electron-phonon interactions. Nevertheless, such processes in silicon and germanium have garnered significant attention owing to the expectations for spin orientation using multivalley band structures [1,2], room temperature spin transport [3], and switching between direct/indirect luminescence using the two energy gaps closely located in germanium [4]. The first-principles calculation of photoabsorption in indirect band-gap materials is challenging, as the intricate process requires taking a double sum over the reciprocal space and a much higher computational cost than for the direct band-gap materials [5]. The recent advent in computer technology enabled first-principles calculations of electron-phonon interactions in the electron-phonon Wannier framework [5,6] and nonperturbative approaches using frozen-phonon displacements [7]. Examples of theoretical studies that yielded remarkable findings also include Refs. [8–10].

Among the group IV family of covalent-bonding classical semiconductors, diamond is an attractive material for future high-power high-speed electronics owing to its extraordinarily high values of thermal conductivity, breakdown voltage, and mobility [11–13]. Furthermore, diamond is a promising material for photonics as it exhibits single photon emission from nitrogen-vacancy centers [14,15] and deep ultraviolet emission across the intrinsic band gap, which is suitable for virus sterilization [16]. The electron-phonon renormalization of the direct and indirect band gaps of diamond was theoretically investigated in Refs. [10,17–19] and Refs. [10,19], respectively. This temperature-dependent effect is often neglected in *ab initio* calculations but sizable in materials composed of light atoms, such as diamond [10]. The electron-phonon interaction strengths were recently calculated over the reciprocal space of diamond [20]. Meanwhile, experimental reports regarding the photoabsorption of diamond are limited, whereas classical studies on cleaved diamond with a thickness ranging from 5 to 250 μm by Clark *et al.* have been primarily cited [21].

In this study, we investigate the phonon-assisted optical transitions of excitons in intrinsic diamond both theoretically and experimentally. Excellent agreement was obtained between the absorption spectra calculated based on the phonon coupling strengths from first-principles calculations [20] and the experimental results. To incorporate temperature shift and broadening into the calculations, we developed a pseudo-Voigt function analysis of the derivative of the experimental absorption spectra. Consequently, the absorption coefficient, which is expressed as the sum of contributions from fine-structure states of excitons and four phonon modes, was derived together with an empirical expression beneficial for applications. We theoretically determined the radiative lifetime of excitons through the phonon-assisted recombination to be 1.5 μs, which is consistent with the experimental derivation via independent measurements reported in Ref. [22] and indicates an approximately 10^3 higher radiative rate than in silicon [23].

After describing the experimental procedure in Sec. II, we provide a detailed calculation method of indirect optical transitions in Sec. III. We present the experimental data based on comparison with theory and derive the radiative rate of the indirect excitons in Sec. IV. The conclusions are presented in Sec. V.

II. EXPERIMENT

Intrinsic single-crystal diamond grown by chemical vapor deposition (purchased from Element Six, Ltd. and named samples A, B, and C) was used in the experiment. The thicknesses of samples A, B, and C, qualified by the supplier, were 0.5, 0.3, and 0.05 mm, respectively, with $\pm 10\%$ accuracy. We measured the thickness of samples A and B by observing the cross section using a microscope (Keyence, VHX-6000), while the direct observation of the cross section of sample C was difficult. We measured the interference fringes of infrared

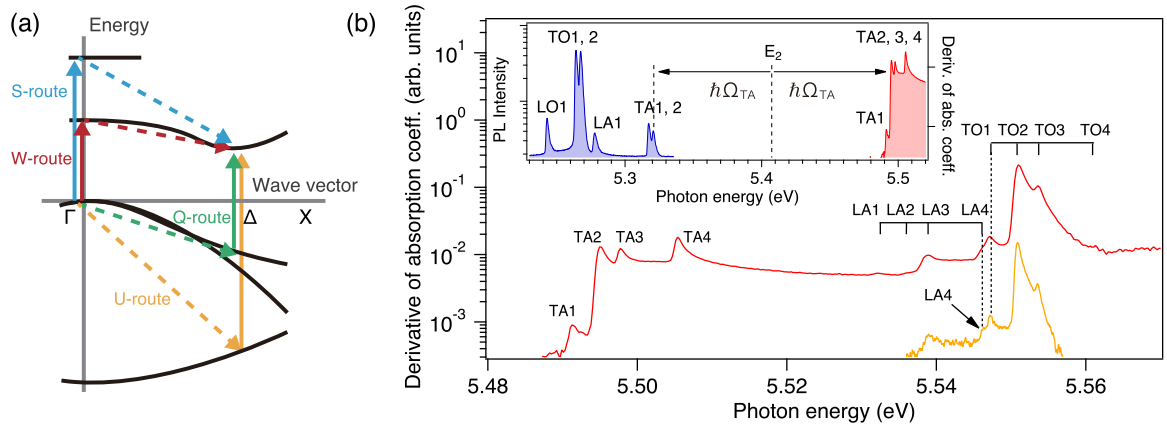

FIG. 1. (a) Schematic of energy bands and possible transition routes of indirect absorption in diamond. Solid arrows correspond to electron-photon interactions, $H_{\rm ep}$; dashed arrows correspond to electron-lattice interactions, $H^j_{\rm el}$. (b) Excitonic fine structure in derivative absorption spectrum measured in sample B at 6 K. Lower curve shows higher-resolution spectrum showing different positions of LA4 and TO1 components. Labels $j\ell$ imply that structure is due to phonon mode j (j = TA, LA, TO, LA) and excitonic fine structure $EX\ell$ ($\ell = 1, 2, 3, 4$). Inset shows comparison with luminescence spectrum (shown in blue) measured at the same temperature.

light at 2400–3200 cm^{-1} in samples B and C using a Fourier-transform infrared spectrometer (Bruker, Vertex 80v), and extracted the refractive index using the measured thickness of sample B. The accurate thickness of sample C was inferred by analyzing the interference fringes using the same refractive index value. Thus, the thickness values for samples A, B, and C, used for the absorption coefficient analysis, were determined to be 532, 318, and 52.8 μm with $\pm 1\%$ accuracy.

A deuterium lamp was used as the light source for the absorption measurements. The light intensity was sufficiently low so that no exciton complexes, such as polyexcitons and electron-hole droplets [22], were created. The transmitted intensity of the light through the sample was measured using a Peltier-cooled charge-coupled device camera at the back of a monochromator with 550-mm focal length. A diffraction grating of 2400 grooves/mm was used to achieve a spectral resolution of $\sim$0.5 meV at a wavelength of 236 nm. When a higher spectral resolution was necessitated, a monochromator with 1500-mm focal length was used with a 2400-grooves/mm grating. The sample was cooled using a closed-cycle helium-gas cryostat from 300 to 6 K.

The absorption spectra were calculated by taking a logarithm of the transmission spectra, which were obtained as the ratio of the spectra with and without the sample in the optical path, and then divided by the sample thickness. Such a spectrum includes a slight offset absorption caused by the reflection loss at the sample surfaces. We corrected this effect by subtracting a straight baseline determined for the transparent energy region (5.15–5.45 eV) for the spectrum obtained at the lowest temperature. We estimated that the possible error in the baseline is ± 0.8 cm^{-1} by comparing spectra obtained from several samples of different thicknesses and at different temperatures.

III. THEORY

A. Transition routes and deformation potentials

The band structure relevant to the optical transitions in diamond is schematically shown in Fig. 1(a). We referred to the linear muffin-tin potential $\boldsymbol{k}\cdot\boldsymbol{p}$ calculations reported by Willatzen *et al.* [24]. The lowest conduction band has a symmetry of Γ_{15} in Bouckaert-Smoluchowski-Wigner (BSW) notation (Γ_4^- in Koster's notation) at the center of the Brillouin zone, originating from the p-type orbital. This band ordering is similar to the case of silicon but different from that of germanium, in which the lowest conduction band originates from the atomic s orbital. The conduction band minimum in diamond is located at 74% of the X point, where the band splits into Δ_1 (lower) and Δ_5 (higher) bands. The second lowest conduction band has a $\Gamma_{2'}$ (Γ_2^-) symmetry at the center of the Brillouin zone. The highest valence band comprises heavy, light, and spilt-off hole bands with $\Gamma_{25'}$ (Γ_5^+) symmetry at the center of the Brillouin zone. It splits into Δ_5 (higher) and Δ_4 (lower) bands at the reciprocal point of the conduction band minimum. The energy of the second valence band of symmetry Γ_1 (Γ_1^+) at the center of the Brillouin zone increases as it approaches to the X point, and the symmetry of the band at the reciprocal point of the conduction band minimum is Δ_1.

The direct band gap of diamond is 7.3 eV while the indirect band gap is 5.5 eV. Owing to the conservation of energy and momentum during the transitions, the absorption of a photon in the range 5.2–6.0 eV (well below the direct band gap) requires the creation or annihilation of at least a single phonon. We considered four routes (W, S, Q, and U) as depicted in Fig. 1(a), because transition routes involving a more remote band do not contribute much to the transition rate because of the large denominator in the second-order perturbation Hamiltonian. The names of the routes follow those conventionally used for silicon [25]. The basic theory describing the indirect optical absorption processes can be found in textbooks [26].

The probability of the transition from an initial state $|i\rangle$ to final state $|f\rangle$ via an intermediate state $|m\rangle$ (with energies of E_i, E_f, and E_m, respectively) is expressed as

$$w^j_{if} = \frac{2\pi}{\hbar}\left|\sum_m \left(S^j_{{\rm CB},m} + S^j_{{\rm VB},m}\right)\right|^2 \delta(E_i - E_f), \qquad (1)$$

where $S^j_{\mathrm{CB},m}$ and $S^j_{\mathrm{VB},m}$ are the generalized optical matrix elements expressed as

$$S^j_{\mathrm{CB},m} = \frac{\langle f|H^j_{\mathrm{el}}|m\rangle\langle m|H_{\mathrm{ep}}|i\rangle}{E_i - E_m} \tag{2}$$

and

$$S^j_{\mathrm{VB},m} = \frac{\langle f|H_{\mathrm{ep}}|m\rangle\langle m|H^j_{\mathrm{el}}|i\rangle}{E_m - E_f}. \tag{3}$$

Here, H^j_{el} represents the electron-lattice (phonon) interaction involving a phonon of mode j [j = transverse acoustic (TA), longitudinal acoustic (LA), transverse optic (TO), and longitudinal optic (LO)], whereas H_{ep} represents the electron-photon interaction. $S^j_{\mathrm{CB},m}$ corresponds to the conduction band scattering of the electrons. We label the two major routes as W and S routes, and they are schematized in Fig. 1(a). $S^j_{\mathrm{VB},m}$ corresponds to the valence band scattering of holes with Q and U routes.

Based on the notation in Refs. [5,7], we define the generalized optical matrix elements of each transition as

$$S^j_r(\hbar\omega) = \frac{P_r g^j_r}{E_r - \hbar\omega}, \tag{4}$$

where r indicates the transition route, $\hbar\omega$ is the photon energy, P_r is the momentum matrix element, g^j_r is the electron phonon interaction matrix element [20], and E_r is the energy difference between the conduction and valence bands in each route corresponding to the denominators in Eqs. (2) and (3), respectively. By considering the possible scattering channels using group theory [27], we found that S^{TA}_W, S^{LA}_W, S^{TO}_W, S^{TA}_Q, S^{LA}_Q, S^{TO}_Q, S^{LO}_Q, S^{LO}_S, S^{TA}_U, S^{TO}_U, and S^{LO}_U have nonzero values.

In Eq. (B4) of Ref. [9], the momentum matrix element P_r is defined by

$$\frac{m_0}{m_{\mathrm{t}}} = 1 + \frac{P_r^2}{m_0}\left[\frac{1}{E_r} + \frac{1}{E_r + \Delta_r}\right] \tag{5}$$

in the case of valence band scattering with spin-orbit energy splitting Δ_r. Therefore, we calculated P_r based on Eq. (5) for Q and U routes. Here, m_0 represents the electron mass at rest, and $m_{\mathrm{t}} = 0.280m_0$ is the transverse effective mass of the electron, which is significantly smaller than the longitudinal effective mass of the electron $m_{\mathrm{l}} = 1.56m_0$, reflecting the anisotropic conduction band [29]. For the W and S routes, we used the electron-photon interaction matrix element from Ref. [24]. The values of E_r, P_r, and Δ_r are summarized in Table I.

The strength of the electron-phonon interaction is described by the deformation potential, $D^j_r(k,q)$. The intravalley deformation potential $D^j_r(k,q)$ from wave vector state k to $k+q$ is related to g^j_r in Eq. (4) by

$$g^j_r(k,q) = \sqrt{\frac{\hbar}{4\Omega^j_q M}}D^j_r(k,q), \tag{6}$$

where Ω^j_q ($=\Omega_j$) is the phonon frequency, and M is the mass of a carbon atom. The electron-phonon interaction matrix elements in diamond, for every momentum transfer allowed for the phonon creation, were recently calculated [20]. Table II summarizes the values of g^j_r from the center of the Brillouin zone to the position of the conduction band minimum. We approximate that phonon frequencies and deformation potentials are wave vector independent around this point. For convenience of comparison with previous simulation studies for diamond [31,32], the values of D^j_r are listed in Table II.

TABLE I. Electronic and band-structure parameters for diamond used for calculation of absorption spectra.

Route (r)	W	S	Q	U
E_r (eV)	7.3[a]	15.3[a]	11.7[a]	14.5[a]
P_r^2/m_0 (eV)	13.6[a]	7.9[a]	15.6[b]	15.6[b]
Δ_r (meV)	6[c]	6[c]	0	0

[a]Extracted from Ref. [24]. P_S and P_W are P and Q parameters in Ref. [24], respectively.
[b]Calculated using Eq. (5).
[c]Reference [30].

B. Phonon energies

Before calculating the absorption coefficients, we present a method to precisely determine the phonon energies $\hbar\Omega_j$. Photoluminescence (PL) is a reverse process of absorption, that occurs at a photon energy shifted by twice the phonon energy from the corresponding phonon-assisted absorption. The inset of Fig. 1(b) shows a comparison of the PL spectrum and the derivative of the absorption spectrum of diamond measured at 6 K. The excitation wavelength for the PL was 225 nm (5.51 eV), which is resonant at the absorption of excitons assisted by TA phonon creation. As presented in Ref. [27], excitons exhibit a fine structure as a combined effect of the spin-orbit interaction, electron-hole exchange, and mass-anisotropy splitting. These effects are the result of the nonspherical part of the excitonic Hamiltonian formulated by Altarelli and Lipari [33,34], and the four fine-structure states are denoted as $EX\ell$ ($\ell = 1, 2, 3, 4$). The lines appearing in the spectra are assigned based on the phonon mode (j = TA, LA, TO, LO) plus index ℓ representing the $EX\ell$ state. Because $EX3$ and $EX4$ lie much higher than $EX1$ compared with the thermal energy of 6 K, they are barely observed in the PL spectrum. In the derivative absorption, structures LA1–LA3 and structures TO1–TO3 can be identified in addition to structures TA1–TA4, which were previously reported in Ref. [27].

TABLE II. Phonon energies ($\hbar\Omega_j$) extracted from analysis of absorption and photoluminescence spectra measured at 6 K, electron-phonon interaction matrix elements (g^j_r) [20], and corresponding deformation potentials (D^j_r).

Phonon mode (j)	TA	LA	TO	LO
$\hbar\Omega_j$ (meV)	87.8	127	141	162
$g^j_{W,S}$ (meV)	70	170	250	0.8
$D^j_{W,S}$ (10^{10} eV/m)	2.2	6.5	10	0.034
$g^j_{Q,U}$ (meV)	38	200	200	290
$D^j_{Q,U}$ (10^{10} eV/m)	1.2	7.6	8.0	12

It is noteworthy that the absorption processes of LA1 and LA2 are optically prohibited and appear only weakly in absorption. The lower curve shows the derivative absorption measured at a higher spectral resolution of 0.35 meV, which shows clear splitting between the structures LA4 and TO1. The signal was accumulated for 8 h and the drift of the center wavelength of the monochromator due to the change in the air temperature was corrected. This observation and newly clarified positions of LA1 and LA2 in the derivative absorption resolved the ambiguity in assigning the LA phonon structure, as reported in Ref. [35].

We evaluated the phonon energies by comparing the absorption and PL edges obtained via spectral fitting [see the horizontal arrows in the inset of Fig. 1(b)]. The PL spectrum was fitted using the function

$$L(\hbar\omega) \propto \sqrt{\hbar\omega + \hbar\Omega_j - E_\ell}\,\exp\left(-\frac{\hbar\omega + \hbar\Omega_j - E_\ell}{k_B T_{\rm eff}}\right), \quad (7)$$

which was convolved with a Gaussian function representing the spectral resolution of 0.5 meV, where $T_{\rm eff}$ is an adjustable parameter representing the effective temperature. For derivative absorption, we used an approximate expression assuming a constant denominator in Eq. (4), i.e.,

$$A'(\hbar\omega) \propto 1/\sqrt{\hbar\omega - \hbar\Omega_j - E_\ell}, \quad (8)$$

which was convolved with a Gaussian function to represent the spectral resolution. A comparison of the PL and absorption edges at $E_\ell \pm \hbar\Omega_j$ for a common ℓ yields the phonon energy. The extracted values of $\hbar\Omega_j$ are listed in Table II. These energies determined by us were more precise than those in Ref. [21]. Additionally, using the E_ℓ values and binding energies ($E_{\rm b1,b2,b3,b4} = 93.8, 90.3, 87.4, 80.2$ meV) of the excitons in the $EX\ell$ state [27,36], we determined the indirect energy gap, $E_{\rm ind} = E_\ell + E_{\rm b\ell} = 5.4979$ eV at 6 K.

C. Discrete and continuum absorption

We calculated the absorption coefficient of diamond including the excitonic effect. Here, we present the analytical forms of the absorption spectra based on a recent model developed in Ref. [28], which avoids the divergence problem near the direct band gap when phonon-assisted optical absorption is treated within standard second-order perturbation theory. We note that this shortcoming is not present when nonperturbative approaches are employed [7].

We assume discrete exciton levels with a principal quantum number n, forming an energy structure analogous to hydrogen series, $E_{\ell,n} = E_\ell + (1 - 1/n^2)E_{\rm b\ell}$. The coefficients for the phonon creation and annihilation processes are expressed as [see Eq. (43) of Ref. [9] and Eq. (48) of Ref. [28]]:

$$\alpha^{\pm}(\hbar\omega) = \sum_{j,\ell}\left\{\frac{(6/4)\times 8\sqrt{2}e^2}{3\pi\rho m_0 c n_{\rm op}}\left(\frac{1}{\hbar\Omega_j}\right)\left(\frac{1}{\hbar\omega}\right)\left(\frac{4\Omega_j M}{\hbar}\right)\left(\frac{F_\ell(\hbar\omega)}{4\pi\epsilon_0 m_0}\right) \times\left(f_j + \frac{1}{2} \pm \frac{1}{2}\right)\frac{R_F M_{\Delta\rm h}^{3/2}}{a_\ell^3}\sum_n \frac{\sqrt{\hbar\omega \mp \hbar\Omega_j - E_{\ell,n}}}{n^3}\right\}, \quad (9)$$

where the degeneracies of six valleys are considered instead of four valleys for germanium and $\sum_h$ in Ref. [9] has been replaced by $\sum_\ell$. Here, $\rho = 3.51\times10^3$ kg m^{-3} is the density of diamond, c is the speed of light, $n_{\rm op} = 2.69$ is the refractive index of diamond, and $f_j = [\exp(\hbar\Omega_j/k_B T) - 1]^{-1}$ is the phonon occupation number. $M_{\Delta\rm h} = m_\Delta + m_{\rm h}$ is the excitonic translational mass in the spherical exciton model [9], where $m_\Delta = 3m_{\rm l}m_{\rm t}/(2m_{\rm l} + m_{\rm t}) = 0.385m_0$ is the electron effective mass at the conduction band minimum and $m_{\rm h} = 3/(1/m_{\rm lh} + 1/m_{\rm hh} + 1/m_{\rm so}) = 0.375m_0$ is the hole effective mass with $m_{\rm hh} = 0.667m_0$ (heavy hole), $m_{\rm lh} = 0.260m_0$ (light hole), and $m_{\rm so} = 0.375m_0$ (split-off hole) [29]. Inclusion of the parameter R_F in Eq. (9), set as the only adjustable parameter in our calculations, is to effectively account for the correction to the excitonic translational mass by the nonspherical part of the excitonic Hamiltonian reflecting anisotropy of the conduction valleys and mixing between valence bands [9] (see the Appendix). $a_\ell = e^2/(8\pi\epsilon_{\rm st}E_{\rm b\ell}) \simeq 1.3$ nm is the Bohr radius of the excitons with the static dielectric constant $\epsilon_{st} = 5.7\epsilon_0$. The sum over n was taken up to $n = 10$ considering the convergence of $1/n^3$.

The coupling coefficients $F_\ell(\hbar\omega)$ for each exciton state can be calculated using the matrix elements $S_r^j(\hbar\omega)$ as follows:

$$\begin{aligned} F_1(\hbar\omega) &= 0,\\ F_2(\hbar\omega) &= A + C,\\ F_3(\hbar\omega) &= B + D + E,\\ F_4(\hbar\omega) &= (A + B + C + D + E)/2, \end{aligned} \quad (10)$$

where

$$\begin{aligned} A^{\rm TA(TO)} &= 8/3\left|S_W^{\rm TA(TO)} + S_Q^{\rm TA(TO)}\right|^2,\\ B^{\rm TA(TO)} &= 8/3\left|S_W^{\rm TA(TO)} + S_U^{\rm TA(TO)}\right|^2,\\ C^{\rm LO} &= 4/3\left|S_S^{\rm LO} + S_U^{\rm LO}\right|^2,\\ D^{\rm LO} &= 8/3\left|S_S^{\rm LO} + S_Q^{\rm LO}\right|^2,\\ E^{\rm LA} &= 8/3\left|S_W^{\rm LA} - S_Q^{\rm LA}\right|^2, \end{aligned} \quad (11)$$

as derived in Ref. [27] using slightly different notations: $W_{\rm TA(TO)} = 2S_W^{\rm TA(TO)}$, $Q_{\rm TA(TO)} = 2S_Q^{\rm TA(TO)}$, $U_{\rm TA(TO)} = \sqrt{2}S_U^{\rm TA(TO)}$, $S_{\rm LO} = \sqrt{3}S_S^{\rm LO}$, $U_{\rm LO} = S_U^{\rm LO}$, $Q_{\rm LO} = 2S_Q^{\rm LO}$, $W_{\rm LA} = \sqrt{2}S_W^{\rm LA}$, and $Q_{\rm LA} = -2S_Q^{\rm LA}$ [37].

In addition to the discrete exciton states, we included the absorption due to excitons in the continuum states. According to Eqs. (29) and (55) of Ref. [28], the continuum absorption is expressed as

$$\alpha_{\rm cont}^{\pm}(\hbar\omega) = \sum_j\left\{\frac{(6/4)e^2}{3\pi\hbar^2 m_o\rho c n_{\rm op}}\left(\frac{1}{\hbar\Omega_j}\right)\left(\frac{1}{\hbar\omega}\right)\left(\frac{4\Omega_j M}{\hbar}\right) \times\left(\frac{\sum_\ell F_\ell(\hbar\omega)m_{\rm h\ell}^{3/2}}{4\pi\epsilon_0 m_0}\right)\left(f_j + \frac{1}{2} \pm \frac{1}{2}\right)m_{\rm t}m_{\rm l}^{1/2}\,T_j^{\pm}(\hbar\omega)\right\} \quad (12)$$

and

$$T_j^{\pm}(\hbar\omega) = \left(\frac{8}{\pi}\right)\int_0^{\hbar\omega - E_{\rm ind} \mp \hbar\Omega_j} dx \frac{\pi\sqrt{R'_{\rm y}}\exp(\pi\sqrt{R'_{\rm y}/x})}{\sinh(\pi\sqrt{R'_{\rm y}/x})} \times\sqrt{\hbar\omega - E_{\rm ind} \mp \hbar\Omega_j - x}, \quad (13)$$

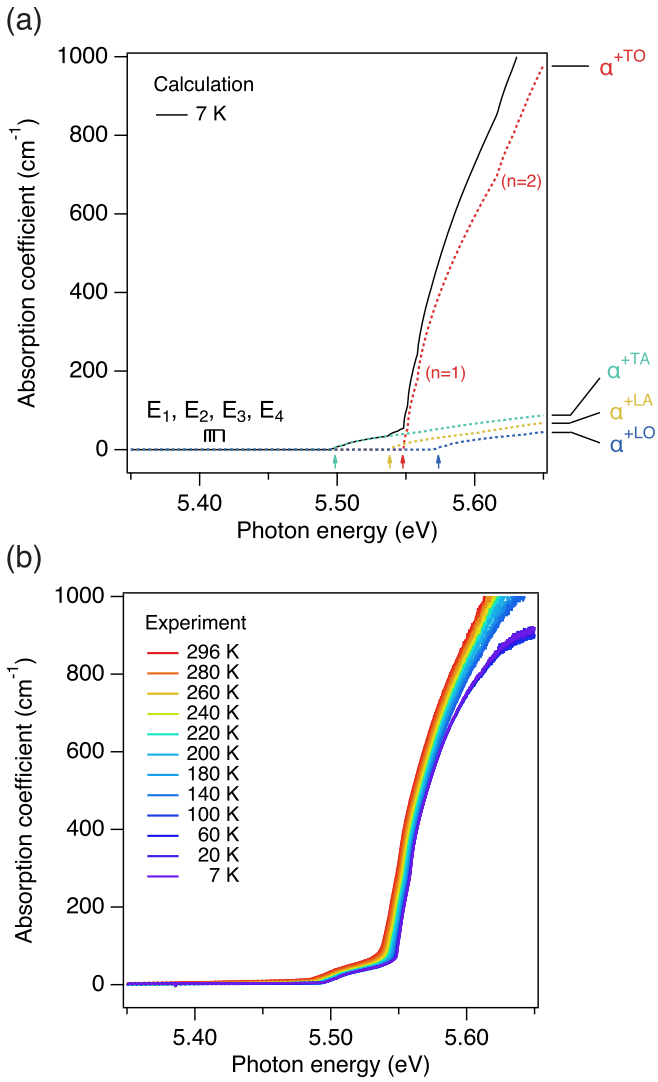

FIG. 2. (a) Calculated absorption coefficients of diamond at 7 K. Dashed lines show components originating from different phonon modes. Bracket indicates positions of excitonic fine structure. (b) Absorption spectra measured in sample C at various temperatures.

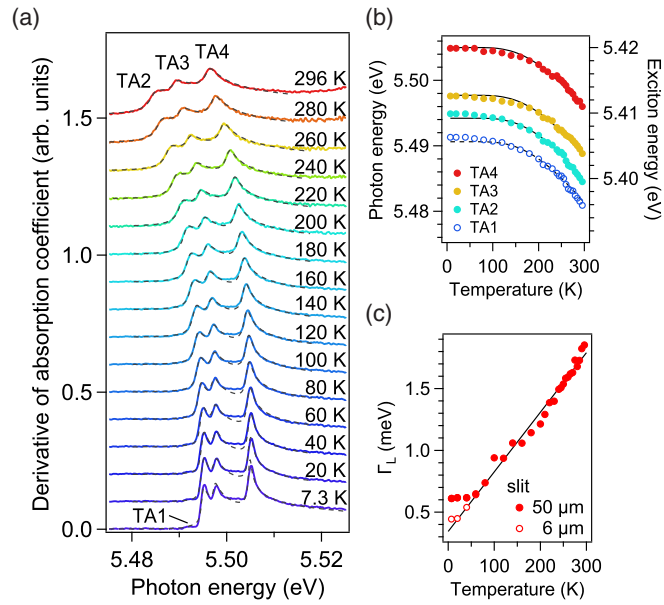

FIG. 3. (a) Derivative of absorption spectra around TA phonon-assisted transition of excitons in sample A at various temperatures. Dashed lines show fitting functions using convolution of Eq. (8) by Eq. (14). (b) Temperature dependence of extracted energy positions of exciton fine structure. Left axis shows directly measured positions, which is the sum of exciton and phonon energies, whereas right axis shows exciton energies E_1, E_2, E_3, and E_4. Points for E_1 (open circles) are estimated by shifting E_2 by 3.6 meV, which is the separation determined at the lowest temperature. Lines are fitting functions shown in Eq. (17). (c) Temperature dependence of Γ_L extracted from pseudo-Voigt fitting. Data points from two different slit settings in monochromator are shown.

where $T_j^{\pm}(\hbar\omega)\times(\hbar\omega - E_{\rm ind} \pm \hbar\Omega_j)^2$ is the excitonic enhancement factor and $R'_y = 86.0$ meV is the average of binding energies $E_{b\ell}$ of optically allowed states ($\ell = 2$–4) [34,36]. The degeneracy factor of 6/4 in Eq. (12) originates from the valley degeneracy of 6 (compared to 4 in germanium) and the split-off hole band is included in the sum $\sum_\ell$. The hole effective masses, $m_{\rm h1} = m_{\rm h2} = 0.667m_0$ (heavy hole), $m_{\rm h3} = 0.260m_0$ (light hole), and $m_{\rm h4} = 0.375m_0$ (split-off hole), were taken from Ref. [29].

IV. RESULTS AND DISCUSSION

A. Excitonic absorption at low temperature

By substituting $F_\ell(\hbar\omega)$ and the other parameters explained in the previous section into Eq. (9), the absorption spectrum of the excitons was calculated using $R_F = 5.0$ chosen as detailed in Fig. 4(b). The results for $T = 7$ K are shown in Fig. 2(a), whereas the experimental data are shown in Fig. 2(b). The overall spectral shape and absolute value of the coefficients were consistent between the calculation and experiment. The calculations revealed that the coefficients of the respective phonon modes appeared in the ratio of TA:LA:TO:LO= 0.07:0.06:1:0.06. This is consistent with the TO lines appearing approximately ten times stronger than other phonon lines in the PL spectrum as well as the ratio of the bound excitons in boron-doped diamond (TA:TO:LO = 0.09:1:0.08) [38]. The strongest coupling of excitons with TO phonon modes was confirmed, implying the dominance of the W route of electron scattering in the exciton-phonon interaction. This is in contrast with the case of germanium (silicon), in which coupling with the LA (LO/TO) phonon is dominant at cryogenic temperatures.

The experimental results at various temperatures are shown in Fig. 2(b). The temperature effect is minor and difficult to clarify in this energy range. More details are discussed in the next subsection.

B. Temperature shift and broadening

Figure 3(a) shows a plot of the derivatives of the absorption spectra of TA-phonon assisted transitions of excitons at various temperatures. The energy shift and broadening effect with temperature were clearly observed, although not considered in the calculation for Fig. 2(a).

The absorption spectra broadened with increasing temperature. This is considered to be due to the homogeneous width increasing with the enhanced phonon scattering rate. To separate this homogeneous width (Lorentzian) and the width originating from the instrumental function of the monochromator (Gaussian), spectral fitting was performed using a pseudo-Voigt function as a convolution function. The pseudo-Voigt function is expressed as follows:

$$f_{\mathrm{pV}}(x) = (1-\eta) f_{\mathrm{G}}(x, \Gamma_{\mathrm{G}}) + \eta f_{\mathrm{L}}(x, \Gamma_{\mathrm{L}}), \tag{14}$$

where $f_{\mathrm{G}}(x, \Gamma_{\mathrm{G}})$ and $f_{\mathrm{L}}(x, \Gamma_{\mathrm{L}})$ are normalized Gaussian and Lorentzian functions with the full width at half the maximum of Γ_{G} and Γ_{L}, respectively. Here, η is a parameter that determines the ratio of the Lorentzian and Gaussian functions and is approximated as [39]

$$\eta = 1.366\,03\left(\frac{\Gamma_{\mathrm{L}}}{\Gamma}\right) - 0.477\,19\left(\frac{\Gamma_{\mathrm{L}}}{\Gamma}\right)^2 + 0.111\,16\left(\frac{\Gamma_{\mathrm{L}}}{\Gamma}\right)^3, \tag{15}$$

where

$$\Gamma = \left(\Gamma_{\mathrm{G}}^5 + 2.692\,69\Gamma_{\mathrm{G}}^4\Gamma_{\mathrm{L}} + 2.428\,43\Gamma_{\mathrm{G}}^3\Gamma_{\mathrm{L}}^2 + 4.471\,63\Gamma_{\mathrm{G}}^2\Gamma_{\mathrm{L}}^3 + 0.078\,42\Gamma_{\mathrm{G}}\Gamma_{\mathrm{L}}^4 + \Gamma_{\mathrm{L}}^5\right)^{1/5}. \tag{16}$$

By fitting the derivative of the absorption spectra shown in Fig. 3(a) using the convolution of Eq. (8) with Eq. (14), we obtained the energy positions of each structure. The fitting functions are shown by dashed lines, which indicated good agreement with the derivative of the measured spectra. Figure 3(b) shows the temperature dependence of each energy position. These excitonic energies are expressed as $E_\ell = E_{\mathrm{ind}} - E_{\mathrm{b}\ell}$ when using the indirect band-gap energy E_{ind} and the excitonic binding energies, $E_{\mathrm{b}\ell}$. E_{ind} shifts with temperature with a Bose-Einstein type variation, as follows [40]:

$$E_{\mathrm{ind}}(T) = E_{\mathrm{ind}}(0) - \frac{a\theta}{\exp(\theta/T) - 1}, \tag{17}$$

where $E_{\mathrm{ind}}(0)$ is the zero-temperature value, and a and θ are parameters. The measured energy values were well reproduced by assuming temperature-independent binding energies $E_{\mathrm{b}\ell}$, $E_{\mathrm{ind}}(0) = 5.4979$ eV, $a = 0.13$ meV/K, and $\theta = 724$ K. The best-fit functions, obtained after a global fitting assuming common temperature dependencies for E_2, E_3, E_4, are shown as solid lines. This plot shows that the analysis of the absorption spectra is more suitable for revealing the excitonic fine structure over a wider temperature range, as *EX*3 and *EX*4 do not exist in the PL spectra at low temperatures [27]. The extracted temperature dependence using Eq. (17) agrees with that derived by the first-principles calculations presented in Ref. [19] ($a = 0.35$ meV/K and $\theta = 1333$ K) or Ref. [10] ($a = 0.44$ meV/K and $\theta = 1539$ K) within 2- or 5-meV difference, respectively, below 300 K.

Figure 3(c) shows the temperature dependence of Γ_{L} extracted from the pseudo-Voigt function fits. The instrumental width at the monochromator was ~0.6 meV with the 50-μm slit, thereby limiting the apparent width below 60 K. We reduced the monochromator slit to 6 μm and resolved the Γ_{L} values to below 0.45 meV at lower temperatures. In general, the temperature dependence of a homogeneous width is expressed as

$$\Gamma_{\mathrm{L}}(T) = \Gamma(0) + d_{\mathrm{ac}}T + \frac{d_{\mathrm{op}}}{\exp(\theta_{\mathrm{ph}}/T) - 1}. \tag{18}$$

The first term represents a constant, and the second (third) term represents broadening due to acoustic (optical) phonon scattering. Because acoustic phonon scattering is dominant in the low-temperature region, fitting was performed to the second term of Eq. (18). Consequently, we obtained $\Gamma(0) = 0.34$ meV and $d_{\mathrm{ac}} = 4.8$ μeV/K. The latter value is relatively large compared with the values reported for III–V and II–VI compound semiconductors, for which a coefficient smaller than 1 μeV/K was primarily reported [41].

C. Continuum absorption

The upper panel of Fig. 4(a) shows the measured absorption spectra (without differentiation) at various temperatures in an expanded energy range. The lower panel shows the calculated spectra by including the temperature-dependent energy shift and broadening. The agreement between the data and calculation improved significantly by this precise analysis. In addition, we examined the absorption due to unbound excitons in the continuum states, assisted by the creation or annihilation of a phonon, by calculating Eq. (12). Continuum absorption begins to appear with the annihilation of the TA phonon at 5.410 eV, whose contribution was found to be very small as shown by the dashed lines (red for 296 K and blue for 7 K) in the lower panel of Fig. 4(a).

Figure 4(b) shows the calculated and measured spectra until a high photon energy of 6.0 eV. In addition to the TA phonon-assisted continuum absorption, continuum absorption with TO-phonon creation began at 5.639 eV (at 7 K) with a higher amplitude. The parameter $R_F = 5.0$ has been included in the discrete exciton component, α_{ex}, calculated using Eq. (9). Here, one can see that the value of R_F is determined without ambiguity, as there is no overlap between the discrete and continuum absorption below 5.63 eV, and each component has obviously different frequency dependence. It is noteworthy that the discrete excitonic absorption (indicated by the dotted lines) deviated slightly from the square-root frequency dependence at high energies owing to the frequency-dependent denominators included in the coefficients S_r^j. The continuum absorption (dashed line) was similar to the classical expression [42] $(\hbar\omega)^{3/2}$.

For the separation between the absorption coefficients of the discrete exciton and continuum origins, we attempted fitting using two components, as follows:

$$\alpha_{\mathrm{sum}}(\hbar\omega) = \sum_{n=1,2} \frac{\overline{A}_{\mathrm{ex}}}{n^3}\sqrt{\hbar\omega - \overline{E}_{\mathrm{ex}} - \left(1 - \frac{1}{n^2}\right)R_y'} + \overline{A}_{\mathrm{cont}}(\hbar\omega - \overline{E}_{\mathrm{cont}})^{3/2}, \tag{19}$$

where $\overline{A}_{\mathrm{ex}}$ and $\overline{E}_{\mathrm{ex}}$ are the *effective* amplitude and position of the excitonic absorption, respectively, averaging the phonon modes and excitonic fine structure; $\overline{A}_{\mathrm{cont}}$ and $\overline{E}_{\mathrm{cont}}$ represent the dominant TO structure of the continuum absorption. The dash-dotted line is the best-fit function for

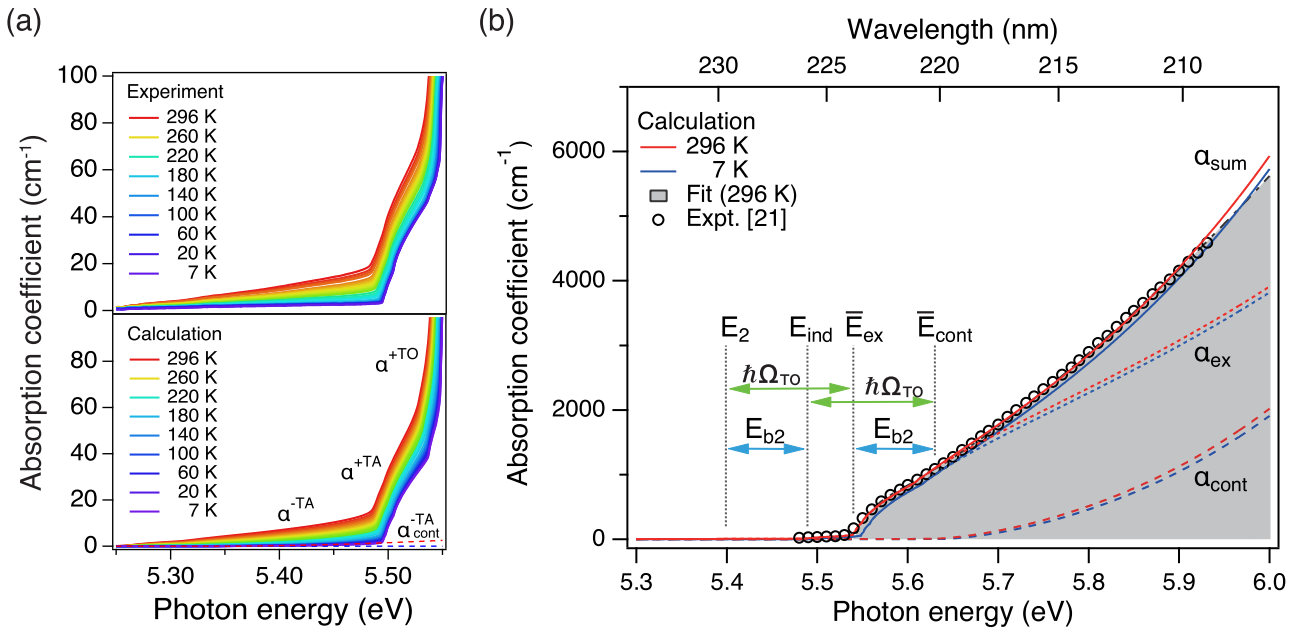

FIG. 4. (a) Measured (upper panel) and calculated (lower panel) spectra in region of TA-phonon-assisted absorption at various temperatures. Calculations shown by full lines included temperature dependence of indirect band-gap energy $E_{\rm ind}(T)$ and broadening $\Gamma_L(T)$. Continuum absorption is shown by dashed lines (blue for 7 K and red for 296 K), which were not included in full lines. (b) Absorption spectra in wider spectral range. Dotted lines: Absorption due to discrete excitons. Dashed lines: Absorption due to continuum states. Full lines: Sum of two components for 7 and 296 K. Circles: Absorption coefficient measured at room temperature [21]. Dash-dotted line with shading: Fit function by Eq. (19).

296 K with $\overline{A}_{\rm ex} = (3474 \pm 7)\ {\rm cm}^{-1}\,{\rm eV}^{-1/2}$, $\overline{E}_{\rm ex} = (5.5424 \pm 0.0002)$ eV, $\overline{A}_{\rm cont} = (1.342 \pm 0.003)\times 10^4\ {\rm cm}^{-1}\,{\rm eV}^{-3/2}$, and $\overline{E}_{\rm cont} = (5.6319 \pm 0.0007)$ eV. For simplicity, the sum over n was taken only for $n = 1$ and 2. This empirical expression almost overlaps with the $\alpha_{\rm sum}$ represented by the red full line and the experimental absorption spectrum from Ref. [21] represented by the circles. The contribution of the continuum absorption was found to reach 50% of the discrete excitonic absorption at 6.0 eV. As indicated by arrows in Figure, $\overline{E}_{\rm ex} \simeq E_2 + \hbar\Omega_{\rm TO}$ was confirmed, showing that the absorption edge is dominated by the coupling between the TO phonon and the $EX2$ state.

D. Rate of phonon-assisted radiative recombination

To date, few attempts were made to determine the radiative rate of the TO-phonon-assisted luminescence of excitons in intrinsic diamond, which dominates the spectrum in the deep ultraviolet region. In Ref. [43], the absorption spectrum and photoluminescence decay were measured at 83 K. The number of incoming photons was estimated based on the absorption coefficient. The number of emitted photons was counted via calibration with the photon counts of the dye laser light to account for the detection sensitivity. The ratio of these two quantities yielded the quantum efficiency. Subsequently, the measured decay time was divided by this efficiency, resulting in a radiative lifetime of 2.3 μs. Because of electron-hole-droplet formation at this temperature, a few counts might have been overlooked [22]. This can cause an underestimation of the quantum efficiency and hence, an overestimation of the radiative lifetime. Being consistent with this interpretation, we recently reported a slightly shorter radiative lifetime of excitons (1.4–1.8 μs) [22] based on an analysis of the measured temperature dependence of exciton lifetime considering the diffusion effect. Herein, we propose to determine the radiative rate based on the absorption derived above, using the principle of detailed balance as proposed by van Roosbroeck and Shockley [44]. Namely, we consider the rate of the phonon-assisted luminescence process using a detailed balance with the inverse process [45].

The rate of photon absorption for exciton creation with the assistance of phonon annihilation is expressed as

$$\frac{c}{n_{\rm op}}\rho_p(\hbar\omega) f_p(\hbar\omega) a_j(\epsilon) f_j(\hbar\Omega_j)[1 + f_x(E_\ell + \epsilon)], \qquad (20)$$

where $\rho_p(\hbar\omega) = n_{\rm op}^3\omega^2/(\hbar\pi^2c^3)$ is the photon density of states, $\epsilon = \hbar\omega + \hbar\Omega_j - E_\ell$ is the exciton kinetic energy, $a_j(\epsilon) f_j(\hbar\Omega_j) = \alpha_j^-(\hbar\omega)$ is the absorption coefficient, and f is the occupation number (with the subscript p for photon, j for phonon, and x for exciton). Because of the large phonon energies in diamond and the low occupation numbers ($f_j \ll 1$), this absorption process appears extremely weak. The amplitude $a_j(\epsilon)$ can be evaluated based on the absorption coefficient $\alpha_j^+(\hbar\omega) = a_j(\epsilon)[1 + f_j(\hbar\Omega_j)]$ for phonon creation, which appears at an energy shifted by $+2\hbar\Omega_j$ [45,46]. Meanwhile, the rate of exciton luminescence with the assistance of phonon creation is expressed as

$$\gamma_j(\hbar\omega) g_x(\epsilon) f_x(E_\ell + \epsilon)[1 + f_j(\hbar\Omega_j)][1 + f_p(\hbar\omega)]. \qquad (21)$$

These two rates should balance, and the luminescence rate is expressed as

$$\gamma_j(\hbar\omega) = \frac{c}{n_{\rm op}} \frac{\rho_p(\hbar\omega) a_j(\epsilon)}{g_x(\epsilon)} \times \frac{1+f_x(E_\ell+\epsilon)}{f_x(E_\ell+\epsilon)} \frac{f_j(\hbar\Omega_j)}{1+f_j(\hbar\Omega_j)} \frac{f_p(\hbar\omega)}{1+f_p(\hbar\omega)}, \quad (22)$$

which can be simplified to

$$\gamma_j(\hbar\omega) = \frac{n_{\rm op}^2(\hbar\omega)^2}{\pi^2 c^2 \hbar^3} \frac{a_j(\epsilon)}{g_x(\epsilon)}. \quad (23)$$

Using the expression for the density of states of the exciton, $g_x(\epsilon) = \frac{g_0 R_F}{4\pi^2\hbar^3}(2M_{\Delta\rm h})^{3/2}\sqrt{\epsilon}$ and $a_j(\epsilon) \simeq \alpha_j^+(\hbar\omega) = \overline{A}_j\sqrt{\epsilon}$, yields

$$\gamma_j(\hbar\omega) \simeq \sqrt{2}\frac{n_{\rm op}^2}{c^2} \frac{(\hbar\omega)^2}{g_0 R_F M_{\Delta\rm h}^{3/2}} \overline{A}_j, \quad (24)$$

where $g_0 = 6\times(1+2+3) = 36$ includes degeneracies of the valleys and optically allowed exciton states, i.e., nondegenerate *EX*2, doubly degenerate *EX*3, and triply degenerate *EX*4 [27]. Substituting $\overline{A}_j = \overline{A}_{\rm ex} = 3474\ {\rm cm}^{-1}\,{\rm eV}^{-1/2}$ from Eq. (19) and $\hbar\omega = 5.27$ eV (at the peak of the TO-phonon assisted luminescence of the highest intensity) yields $\gamma_{\rm ex} = 6.8\times10^5\ {\rm s}^{-1}$ and $\gamma_{\rm ex}^{-1} = 1.5\ \mu$s. The extracted value matches the radiative lifetime determined using the extended surface recombination model [22] on the temperature dependent exciton lifetime.

It would be worthwhile comparing the obtained value with the radiative lifetime in silicon from a general perspective. Similar to the case of bound excitons [47], the factor $(\hbar\omega)^2$ in Eq. (23) enhances the radiative recombination in diamond compared to silicon. Furthermore, the electron-phonon coupling strengths in diamond are approximately three to five times stronger than in silicon [8,20] and they are squared in Eq. (9). This further promotes the radiative recombination of phonon-assisted recombination in diamond. These factors may explain the 10^3-fold difference between the microsecond radiative lifetime in diamond and a millisecond one known for silicon [23]. Because the phonon-assisted exciton luminescence dominates the ultraviolet emission of high-quality intrinsic diamond, this relatively high radiative rate makes diamond much better suited for optoelectronics applications than other indirect band-gap materials of low radiative rates.

V. CONCLUSIONS

We investigated the phonon-assisted optical transitions of excitons in intrinsic diamond both theoretically and experimentally. Excellent agreement with experiments was indicated for the absorption spectra of excitons calculated using the phonon coupling strengths derived from first-principles calculations using just a single adjustable parameter to include the nonspherical correction to the exciton translational mass. We successfully reproduced the temperature dependence by including shift and broadening via the pseudo-Voigt function analysis developed for the derivative of the experimental spectra. Our calculation enabled the separation of multiple processes overlapped in the experimental spectra, such as absorption to discrete and continuum exciton states and absorption involving different phonon modes. This led to theoretical derivation of the radiative recombination rate of excitons in diamond, discovered to be consistent with our experimental value [22] and much higher than in silicon.

This study strengthens the understanding of the optical processes in diamond quantitatively, instead of qualitatively, based on first principles. The empirical expression in Eq. (19) is simple and should particularly benefit researchers in various area of diamond research, including device applications [48]. From a theoretical perspective, our findings widen the generality of the second-order perturbation theory regarding electron-phonon interactions in materials important for optoelectronics and power electronics, whose detailed discussions have been limited to spintronics materials, such as silicon, germanium, and related alloys hitherto.

ACKNOWLEDGMENTS

We thank I. Akimoto (Wakayama University) for providing the 0.3-mm-thick sample and K. Tanaka (Kyoto University) for use of the optical microscope and Fourier-transform infrared spectrometer. This study was partially supported by the JSPS bilateral project (Project No. 120209919) and JSPS KAKENHI (Grants No. 17H02910 and No. 19K21849).

APPENDIX: SPHERICAL APPROXIMATION

The electron kinetic energy term of an excitonic Hamiltonian is described as

$$H_{\rm e} = \hbar^2\left(\frac{k_x^2}{2m_x} + \frac{k_y^2}{2m_y} + \frac{k_z^2}{2m_z}\right). \quad (A1)$$

For an electron in an anisotropic conduction band minimum described with effective masses $m_x = m_y = m_{\rm t}$ and $m_z = m_{\rm l}$, the Hamiltonian can be separated into spherically and nonspherically symmetric parts [33]. The former is expressed with an effective mass of $m_{\rm sph,e} = (2/m_{\rm t} + 1/m_{\rm l})/3$, and $m_{\rm sph,e} = 0.385m_0$ for diamond. The Hamiltonian for a hole is written as

$$H_{\rm h} = \hbar^2\left(\frac{k_x^2+k_y^2+k_z^2}{2m_i}\right), \quad (A2)$$

with i = hh, lh, and so, respectively for the heavy-hole, light-hole and split-off bands, which are assumed to be isotropic. The three hole bands mix each other by the nonspherical part of the Hamiltonian, and treated with an average effective mass of $m_{\rm sph,h} = 3/(1/m_{\rm hh} + 1/m_{\rm lh} + 1/m_{\rm so})$, which yields $m_{\rm sph,h} = 0.375m_0$ for diamond. These relations indicate that a lighter mass contributes more to the energy and has a larger weight in the average spherical masses. In the main text, $m_{\rm sph,e}$ and $m_{\rm sph,h}$ were referred to as m_Δ and $m_{\rm h}$, respectively. The translational effective mass in the spherical approximation was given by $M_{\Delta\rm h} = m_\Delta + m_{\rm h} = 0.760m_0$.

Meanwhile, the density of states contains the factor $(m_x m_y m_z)^{1/2} = m_{\rm t}\sqrt{m_{\rm l}}$, and hence $m_{\rm dos,e} = (m_{\rm t}^2 m_{\rm l})^{1/3}$ is conventionally defined for an anisotropic electron. Similarly, $m_{\rm dos,h} = (m_{\rm hh}^{3/2}/3 + m_{\rm hh}^{3/2}/3 + m_{\rm so}^{3/2}/3)^{2/3}$ is used for an average density of states for a sphericalized hole band. Both of

$m_{\mathrm{dos,e}} = 0.496m_0$ and $m_{\mathrm{dos,h}} = 0.450m_0$ are obviously heavier than $m_{\mathrm{sph,e}}$ and $m_{\mathrm{sph,h}}$ in diamond. To correct the underestimate of the joint density of states for excitons when using the sphericalized effective masses, the enhancement parameter R_F was introduced in Ref. [9]. We extend the definition to include the split-off hole band for diamond and obtained $R_F = (m_{\mathrm{dos,e}}m_{\mathrm{dos,h}})^{3/2}/(m_{\mathrm{sph,e}}m_{\mathrm{sph,h}})^{3/2} \sim 2$.

The above correction takes account of the electron anisotropy with holes approximated by isotropic bands. The exciton translational masses with *anisotropic* hole bands were discussed by Kane in the limit of a large spin-orbit energy splitting [49]. The limit is not exactly valid for diamond, but we estimated a translational exciton mass of $M \sim 3M_{\Delta\mathrm{h}}$ ($M^{3/2} \sim 5M_{\Delta\mathrm{h}}^{3/2}$) along the [001] direction when neglecting the split-off band. Furthermore, the small spin-orbit interaction in diamond induces mixing between the split-off and other hole bands, whose effects were not incorporated in the above and previous calculations for silicon and germanium of large spin-orbit energy splitting. The perturbative $\boldsymbol{k}\cdot\boldsymbol{p}$ Hamiltonian for anisotropic hole bands [50,51] predicts enhancement of the hole masses with increasing wave vector, particularly for [110] and equivalent directions. Although a quantitative estimate of this effect is out of the scope of this paper, we consider that R_F larger than 2 is reasonable.

[1] P. Li, D. Trivedi, and H. Dery, Spin-dependent optical properties in strained silicon and germanium, Phys. Rev. B **87**, 115203 (2013).

[2] A. Ferrari, F. Bottegoni, S. Cecchi, G. Isella, and F. Ciccacci, Optical spin orientation in group-IV heterostructures, J. Appl. Phys. **113**, 17C504 (2013).

[3] S. Dushenko, M. Koike, Y. Ando, T. Shinjo, M. Myronov, and M. Shiraishi, Experimental Demonstration of Room-Temperature Spin Transport in n-type Germanium Epilayers, Phys. Rev. Lett. **114**, 196602 (2015).

[4] C. Rinaldi, M. Cantoni, M. Marangoni, C. Manzoni, G. Cerullo, and R. Bertacco, Wide-range optical spin orientation in Ge from near-infrared to visible light, Phys. Rev. B **90**, 161304(R) (2014).

[5] J. Noffsinger, E. Kioupakis, C. G. Van de Walle, S. G. Louie, and M. L. Cohen, Phonon-Assisted Optical Absorption in Silicon from First Principles, Phys. Rev. Lett. **108**, 167402 (2012).

[6] S. Ponce, E. R. Margine, C. Verdi, and F. Giustino, EPW: Electron-phonon coupling, transport and superconducting properties using maximally localized Wannier functions, Comput. Phys. Commun. **209**, 116 (2016).

[7] M. Zacharias, C. E. Patrick, and F. Giustino, Stochastic Approach to Phonon-Assisted Optical Absorption, Phys. Rev. Lett. **115**, 177401 (2015).

[8] N. Tandon, J. D. Albrecht, and L. R. Ram-Mohan, Electron-phonon interaction and scattering in Si and Ge: Implications for phonon engineering, J. Appl. Phys. **118**, 045713 (2015).

[9] J. Menendez, D. J. Lockwood, J. C. Zwinkels, and M. Noel, Phonon-assisted optical absorption in germanium, Phys. Rev. B **98**, 165207 (2018).

[10] M. Zacharias and F. Giustino, One-shot calculation of temperature-dependent optical spectra and phonon-induced band-gap renormalization, Phys. Rev. B **94**, 075125 (2016).

[11] J. Isberg, J. Hammersberg, E. Johansson, T. Wikström, D. Twitchen, A. Whitehead, S. Coe, and G. Scarsbrook, High carrier mobility in single-crystal plasma-deposited diamond, Science **297**, 1670 (2002).

[12] P. Volpe, J. Pernot, P. Muret, and F. Omnes, High hole mobility in boron doped diamond for power device applications, Appl. Phys. Lett. **94**, 092102 (2009).

[13] I. Akimoto, Y. Handa, K. Fukai, and N. Naka, High carrier mobility in ultrapure diamond measured by time-resolved cyclotron resonance, Appl. Phys. Lett. **105**, 032102 (2014).

[14] E. Bourgeois, A. Jarmola, P. Siyushev, M. Gulka, J. Hruby, F. Jelezko, D. Budker, and M. Nesladek, Photoelectric detection of electron spin resonance of nitrogen-vacancy centres in diamond, Nat. Commun. **6**, 8577 (2015).

[15] P. Siyushev, M. Nesladek, E. Bourgeois, M. Gulka, J. Hruby, T. Yamamoto, M. Trupke, T. Teraji, J. Isoya, and F. Jelezko, Photoelectrical imaging and coherent spin-state readout of single nitrogen-vacancy centers in diamond, Science **363**, 728 (2019).

[16] T. Makino, K. Yoshino, N. Sakai, K. Uchida, S. Koizumi, H. Kato, D. Takeuchi, M. Ogura, K. Oyama, T. Matsumoto, H. Okushi, and S. Yamasaki, Enhancement in emission efficiency of diamond deep-ultraviolet light emitting diode, Appl. Phys. Lett. **99**, 061110 (2011).

[17] F. Giustino, S. G. Louie, and M. L. Cohen, Electron-Phonon Renormalization of the Direct Band Gap of Diamond, Phys. Rev. Lett. **105**, 265501 (2010).

[18] S. Ponce, G. Antonius, P. Boulanger, E. Cannuccia, A. Marini, M. Cote, and X. Gonze, Verification of first-principles codes: Comparison of total energies, phonon frequencies, electron-phonon coupling and zero-point motion correction to the gap between ABINIT and QE/Yambo, Comput. Mater. Sci. **83**, 341 (2014).

[19] S. Ponce, Y. Gillet, J. Laflamme Janssen, A. Marini, M. Verstraete, and X. Gonze, Temperature dependence of the electronic structure of semiconductors and insulators, J. Chem. Phys. **143**, 102813 (2015).

[20] N. Tandon, J. D. Albrecht, and L. R. Ram-Mohan, Electron-phonon coupling and associated scattering rates in diamond, Diam. Relat. Mater. **56**, 1 (2015).

[21] C. D. Clark, P. J. Dean, and P. V. Harris, Intrinsic edge absorption in diamond, Proc. R. Soc. London A **277**, 312 (1964).

[22] K. Konishi, I. Akimoto, J. Isberg, and N. Naka, Diffusion-related lifetime and quantum efficiency of excitons in diamond, Phys. Rev. B **102**, 195204 (2020).

[23] D. K. Schroder, *Semiconductor Material and Device Characterization*, 3rd ed. (John Wiley & Sons, Hoboken, New Jersey, 2015).

[24] M. Willatzen, M. Cardona, and N. E. Christensen, Linear muffin-tin-orbital and k·p calculations of effective masses and band structure of semiconducting diamond, Phys. Rev. B **50**, 18054 (1994).

[25] D. L. Smith and T. C. McGill, Temperature dependence of the relative integrated intensities of symmetry-allowed

phonon- assisted exciton emission in Si and Ge, Phys. Rev. B **14**, 2448 (1976).

[26] P. Y. Yu and M. Cardona, *Fundamentals od Semiconductors: Physic and Materials Properties* (Springer-Verlag, Berlin, 1996).

[27] Y. Hazama, N. Naka, and H. Stolz, Mass-anisotropy splitting of indirect excitons in diamond, Phys. Rev. B **90**, 045209 (2014).

[28] J. Menendez, C. D. Poweleit, and S. E. Tilton, Temperature-dependent photoluminescence in Ge: Experiment and theory, Phys. Rev. B **101**, 195204 (2020).

[29] N. Naka, K. Fukai, Y. Handa, and I. Akimoto, Direct measurement via cyclotron resonance of the carrier effective masses in pristine diamond, Phys. Rev. B **88**, 035205 (2013).

[30] C. J. Rauch, Millimeter Cyclotron Resonance Experiments in Diamond, Phys. Rev. Lett. **7**, 83 (1961).

[31] M. Gabrysch, S. Majdi, D. J. Twitchen, and J. Isberg, Electron and hole drift velocity in CVD diamond, J. Appl. Phys. **109**, 063719 (2011).

[32] J. Pernot, P. N. Volpe, F. Omnes, P. Muret, V. Mortet, K. Haenen, and T. Teraji, Hall hole mobility in boron-doped homoepitaxial diamond, Phys. Rev. B **81**, 205203 (2010).

[33] N. O. Lipari and M. Altarelli, Theory of indirect excitons in semiconductors, Phys. Rev. B **15**, 4883 (1977).

[34] T. Ichii, N. Naka, and K. Tanaka, Rotational symmetry breaking on the Rydberg energy spectrum of indirect excitons in diamond studied by terahertz time-domain spectroscopy, Phys. Rev. B (to be published) (2021).

[35] R. Ishii, S. Shikata, T. Teraji, H. Kanda, H. Watanabe, M. Funato, and Y. Kawakami, Intrinsic exciton transitions of isotopically purified ^{13}C studied by photoluminescence and transmission spectroscopy, Jpn. J. Appl. Phys. **59**, 010903 (2020).

[36] T. Ichii, Y. Hazama, N. Naka, and K. Tanaka, Study of detailed balance between excitons and free carriers in diamond using broadband terahertz time-domain spectroscopy, Appl. Phys. Lett. **116**, 231102 (2020).

[37] The phase between two matrix elements in E^{LA} was chosen to best reproduce the experimental ratio of TA2:LA3:TO2 in Fig. 1(b).

[38] Y. Kubo, M. Takahata, S. Temgoua, R. Issaoui, J. Barjon, and N. Naka, Phonon-assisted transitions of bound excitons in diamond: analysis by mirror symmetry, Phys. Rev. B **101**, 205204 (2020).

[39] T. Ida, M. Ando, and H. Toraya, Extended pseudo-Voigt function for approximating the Voigt profile, J. Appl. Cryst. **33**, 1311 (2000).

[40] R. Paessler, Parameter sets due to fittings of the temperature dependencies of fundamental bandgaps in semiconductors, Phys. Status Solidi B **216**, 975 (1999).

[41] S. Rudin, T. L. Reinecke, and B. Segall, Temperature-dependent exciton linewidths in semiconductors, Phys. Rev. B **42**, 11218 (1990).

[42] Y. P. Varshni, Band-to-band radiative recombination in groups IV, VI, and III-V semiconductors (I), Phys. Status Solidi B **19**, 459 (1967).

[43] A. Fujii, K. Takiyama, R. Maki, and T. Fujita, Lifetime and quantum efficiency of luminescence due to indirect excitons in a diamond, J. Lumin **94-95**, 355 (2001).

[44] W. van Roosbroeck and W. Shockley, Photon-radiative recombination of electrons and holes in Germanium, Phys. Rev. **94**, 1558 (1954).

[45] K. E. O'Hara, Relaxation kinetics of excitons in cuprous oxide, Ph.D. thesis, University of Illinois at Urbana-Champaign, 1999.

[46] See pp. 492 and 497 of [42].

[47] Y. Kubo, S. Temgoua, R. Issaoui, J. Barjon, and N. Naka, Radiative lifetime of boron-bound excitons in diamond, Appl. Phys. Lett. **114**, 132104 (2019).

[48] D. Takeuchi, S. Koizumi, T. Makino, H. Kato, M. Ogura, H. Ohashi, H. Okushi, and S. Yamasaki, Negative electron affinity of diamond and its application to high voltage vacuum power switches, Phys. Status Solidi A **210**, 1961 (2013).

[49] E. O. Kane, Exciton dispersion in degenerate bands, Phys. Rev. B **11**, 3850 (1975)

[50] K. Ya. Shtivel'man, Energy spectrum of holes in diamond-type crystals, Sov. Phys. Solid State **2**, 464 (1960).

[51] K. Ya. Shtivel'man, Energy spectrum for holes in diamond type crystals, Sov. Phys. Solid State **2**, 598 (1960).